Available online at www.sciencedirect.com
ScienceDirect
Journal of the European Ceramic Society 29 (2009) 2333–2341
www.elsevier.com/locate/jeurceramsoc

Preparation of barium hexaferrite coatings using atmospheric plasma spraying

Darja Lisjak [a,*], Kirsten Bobzin [b], Katharina Richardt [b], Marion Bégard [b], Giovanni Bolelli [c], Luca Lusvarghi [c], Arto Hujanen [d], Pertti Lintunen [d], Massimo Pasquale [e], Elena Olivetti [e], Miha Drofenik [a], Thomas Schläfer [b]

[a] *Jožef Stefan Institute, Department for Materials Synthesis, Ljubljana, Slovenia*
[b] *Surface Engineering Institute, RWTH Aachen University, Aachen, Germany*
[c] *Department of Materials and Environmental Engineering, University of Modena and Reggio Emilia, Modena (MO), Italy*
[d] *VTT Technical Research Centre of Finland, P.O. Box 1000, FIN-02044 VTT, Finland*
[e] *INRIM, Electromagnetism Division, Turin, Italy*

Received 21 October 2008; received in revised form 21 January 2009; accepted 27 January 2009
Available online 23 February 2009

Abstract

Thick coatings of barium hexaferrite with the compositions $BaFe_{12}O_{19}$ and $BaCoTiFe_{10}O_{19}$ were prepared using atmospheric plasma spraying (APS) technology. The coatings were prepared from pre-reacted powders of the desired composition. The as-deposited coatings were poorly crystallized, but their crystallinity was improved with a subsequent annealing. The crystallization mechanism of the sprayed hexaferrites was studied during annealing up to 1300 °C, using X-ray powder diffraction combined with thermal analysis and with electron microscopy including microanalysis. Single-phase coatings were obtained after annealing treatments at 1100–1300 °C. Their magnetic properties showed that they would be suitable for absorbers at microwave and mm-wave frequencies, depending on the coating phase's composition, the crystallinity and the thicknesses.

Keywords: Ferrites; Thermal spraying; Solid-state reaction; Magnetic properties; Dielectric properties

1. Introduction

Barium hexaferrites are well-known ferrimagnetic materials suitable for various applications, such as motor components, magnetic recording media, microwave and mm-wave devices and absorbers. These absorbers of electromagnetic waves are used to suppress the electromagnetic noise and pollution caused by the ever-increasing exploitation of electromagnetic waves in everyday life, e.g., in electronics, wireless communication, and telecommunications devices.

The basic compound of barium hexaferrites has the chemical composition $BaFe_{12}O_{19}$ and a complex magnetoplumbite structure.[1] The $BaFe_{12}O_{19}$ unit cell is a combination of two structural blocks aligned in the direction of the hexagonal *c*-axis: RSR*S* (* indicates the 180° rotation of the structural block with respect to the *c*-axis). The S block has a spinel structure with cubic closed-packed O ions and Fe ions on its tetrahedral and octahedral sites. The R block is formed of hexagonally closed-packed O ions and one Ba ion. Fe ions occupy the interstitial, tetrahedral, octahedral and bipyramidal sites. The main intrinsic magnetic properties – the saturation magnetization and the magnetocrystalline anisotropy – result from the specific site occupancy of the magnetic Fe ions and from the anisotropic structure. The saturation magnetization of bulk $BaFe_{12}O_{19}$ is 72 emu/g and its anisotropy field is 17 kOe.[1] Both properties can be varied by substituting the Fe ions with other ions. Due to its very high magnetocrystalline anisotropy $BaFe_{12}O_{19}$ exhibits a ferromagnetic resonance at around 50 GHz and is suitable for special mm-wave applications like radar, as the highest losses and the absorption of the electromagnetic waves occur at frequencies close to resonance. For mass-market microwave applications, operating in the 1−10 GHz range the magnetocrystalline anisotropy and the frequency of the ferromagnetic resonance have to be reduced. This is possible with

* Corresponding author. Tel.: +386 1 4773 872; fax: +386 1 251 9385.
E-mail address: darja.lisjak@ijs.si (D. Lisjak).

0955-2219/$ – see front matter © 2009 Elsevier Ltd. All rights reserved.
doi:10.1016/j.jeurceramsoc.2009.01.028

Table 1
Spraying parameters.

Composition	Current (A)	Gas: Ar (SLPM)	Gas: H_2 (SLPM)	Carrier gas (SLPM)	Spray distance (mm)	Grain size (μm)	Substrate
$BaFe_{12}O_{19}$	500	50	6	3.5	130	20–5	Steel
$BaFe_{12}O_{19}$	500	50	6	3.5	130	20–40	Glass
$BaFe_{10}CoTiO_{19}$	400	50	0	3.5	130	60–80	Glass

the substitution of Fe ions by $Me^{II}M^{IV}$, i.e., Me = Mn, Co, Ni, Zn and M = Ti, Sn, Ir, Rh.[2–7]

The demands for the production of microwave absorbers have been increasing steadily. Typical commercial absorbers are in the form of ceramics or polymer composites filled with absorbing powders. These absorbers represent a special element in electronic modules and have only a limited possibility to be adjusted to the various shapes of the components that require electromagnetic protection. However, this can be overcome with the application of spraying technologies for the preparation of absorbent coatings. Spraying technologies are well-known methods for the preparation of coatings on various objects that have a range of geometries.[8,9] Despite this, only a few examples of using spraying for the preparation of electromagnetically active coatings have been reported. Bartuli et al.,[10] for example, used thermal spraying for the preparation of different absorbent coatings based on a combination of lossy conductors, dielectrics and/or NiZn ferrites. However, the final composition of their as-sprayed coatings was not the same as the starting composition in all of the samples. The reason for this was the interaction of the powders with the plasma gas. There have also been a few reports on the use of thermal spray technologies for the preparation of NiZn and MnZn ferrite coatings.[11–13] The as-sprayed coatings were amorphous and subsequent annealing was necessary for the crystallization of the ferrite phases. The same was true for the $BaFe_{12}O_{19}$ coatings prepared from Ba- and Fe-nitrate solutions with inductively coupled plasma technology.[14] However, when the substrate was heated to 600–900 °C during the deposition, the $BaFe_{12}O_{19}$ crystallized together with hematite. In this paper we present the preparation of barium hexaferrite coatings with atmospheric plasma spraying (APS) technology using the feedstock powders with the desired composition. The selected compositions of $BaFe_{12}O_{19}$ and $BaCoTiFe_{10}O_{19}$ are suitable for mm- and microwave absorbers, respectively.[15,16] The crystallization of barium hexaferrites in the APS coatings will be presented and discussed together with their magnetic properties.

2. Experimental procedure

The powders for spraying with the compositions $BaFe_{12}O_{19}$ (Ba hexaferrite) and $BaCoTiFe_{10}O_{19}$ (Ba-CoTi hexaferrite) were synthesized with solid-state reaction from $BaCO_3$ (Merck, 98.5%), Co_3O_4 (Alfa Aesar, 99%), TiO_2 (Alfa Aesar, anatase, 99%) and Fe_2O_3 (NK-α SEW, 99.65%) in 1–2 kg batches. The reagents were homogenized with a Fe/Ba ratio of 11.5 (Ba hexaferrite) and with a stoichiometric ratio of elements (Ba-CoTi hexaferrite) in a water/ethanol slurry for 1 h using a Turbula homogenizer. After drying at 80 °C the powders were calcined at 1100 °C for 6 h (Ba hexaferrite) or 3 h (Ba-CoTi hexaferrite). The as-calcined powders were milled in an attritor for 2 h at 200 rpm, resulting in submicron particles with a relatively homogeneous particle size distribution. Such powders were suitable for agglomeration using the spray-drying process. After this spray drying the powder-agglomerate size was determined using a Lecotract-LT100 (St. Joseph, Michigan, USA) particle size analyzer. The two powder fractions 20−85 μm and 20−40 μm were used for the APS. The $BaFe_{12}O_{19}$ powder was sprayed on steel by APS with an F4 torch from Sulzer Metco, using a plasma composed of argon and hydrogen. The hydrogen has a good thermal conductivity and imparts a higher temperature to the plasma. An additional Ba hexaferrite sample was produced with similar plasma parameters, but was sprayed on glass and with a smaller grain size, 20–40 μm instead of 20–85 μm for the first sample. With respect to the Ba-CoTi hexaferrite sample, in order to keep the temperature as low as possible, the sample was sprayed on glass without hydrogen and with a lower current than for the Ba hexaferrite sample. The spray parameters are listed in Table 1. The as-deposited coatings were annealed at 380–1300 °C for up to 3 h in air. In parallel with this process, the finely ground coatings removed from the substrate were annealed using the same conditions. It was found out that the Fe from the steel substrate reacts with the coating at 600 °C and higher, while the glass substrate proved to be chemically compatible with the coating material. Therefore, the results presented in the subsequent text are obtained from the coatings prepared on glass substrates and/or on powdered coatings.

The synthesis of the powders and the structural evolution of the coatings were monitored with X-ray powder diffraction (XRD) using a D4 Endeavor Diffractometer (Bruker AXS) and an X'Pert PRO MPD Diffractometer (PANalytical). XRD in a combination with thermogravimetric analyses and differential scanning calorimetry (TGA and DSC) with heating and cooling rates of 1 and 5 K/min using a TG/DT analyzer (Netzsch STA 429 and DSC 404 systems) with a Pt crucible was conducted for the investigation of the crystallization mechanism of the $BaFe_{12}O_{19}$. For this investigation the coating was removed from the substrate and finely ground in an agate mortar. The microstructures of the powders and the phase composition of the coatings and of the coatings' cross-sections were observed with the scanning electron microscope (FEI XL30) combined with energy-dispersive X-ray analyses (EDX) for the phase compositions. The coatings were cold-mounted in resin, ground using SiC papers (up to 2500 mesh) and polished using a diamond slurry (down to 0.5 μm). Further SEM observations were also performed on fracture surfaces, prepared by breaking the coated samples in liquid nitrogen. The magnetic properties of the powdered coatings were measured with a Lakeshore 7400

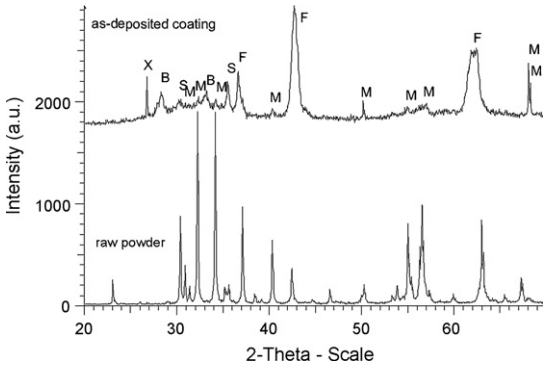

Fig. 1. XRD patterns of the raw Ba hexaferrite powder and the as-deposited coating. M denotes $BaFe_{12}O_{19}$, B denotes $BaFe_2O_4$, S denotes Fe_3O_4, F denotes FeO, X denotes peaks from the substrate. The unmarked peaks of the raw powder all correspond to the $BaFe_{12}O_{19}$ (μPDSM 84-0757).

vibrating-sample magnetometer (VSM) at a maximum field of 1.2 T. The permeability and the permittivity of the samples were obtained from the S-parameters measured with a Vector Network Analyzer (Agilent 8510C VTT). The measurement method is basically the same as described in the 8510 product note.[17] A coaxial sample holder with an inner diameter of 3 mm and an outer diameter of 7 mm was used at frequencies of 0.4–18.0 GHz. The length of the Ba-CoTi hexaferrite sample was 2.16 mm. A standard rectangular waveguide, 1.88 × 3.76 mm, was used at 46–60 GHz. The length of the Ba hexaferrite sample was 0.47 mm. The permeability and the permittivity of the samples were obtained from the measured S-parameters using the transmission line analogy. The transmission-line method itself is broadband, but the inaccuracies in the sample preparation and its dimensions might decrease the accuracy of the measurements or limit the measurement's bandwidth. Bulk samples for the EM measurements were prepared by sintering milled powders at 1300 °C for 3 h with final machining to achieve the required dimensions.

3. Results and discussion

3.1. The Ba hexaferrite coatings

Fig. 1 shows XRD patterns of the Ba hexaferrite feedstock powder and the as-deposited coating. The XRD peaks of the Ba hexaferrite powder all correspond to the $BaFe_{12}O_{19}$ structure, while various structures can be identified in the XRD pattern of the as-deposited Ba hexaferrite coating. The most intense peaks in the XRD pattern fit best to the FeO (wuestite) structure. The other peaks correspond to $BaFe_2O_4$ and Fe_3O_4 (magnetite). Only two minor peaks with very low intensities can be attributed to the $BaFe_{12}O_{19}$. An increased background at low 2-theta angles indicates the presence of an amorphous or poorly crystallized phase. The presence of the $BaFe_2O_4$ and Fe oxides indicates that the crystallization of $BaFe_{12}O_{19}$ from the amorphous melt is not direct. Instead, it follows a similar route

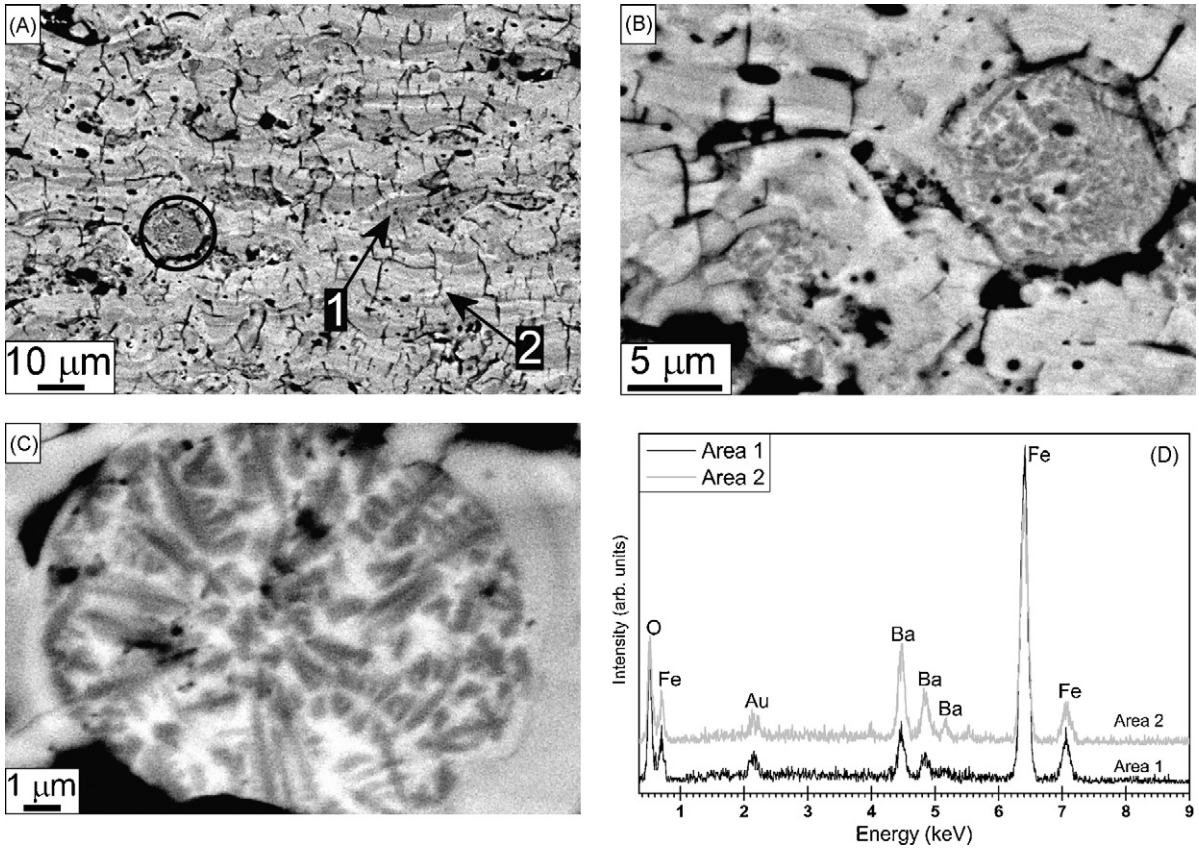

Fig. 2. SEM micrograph (backscattered electrons) of the polished cross-section of the as-deposited Ba hexaferrite coating (A – the circle indicates a spherical inclusion), detailed views of two spherical inclusions (B and C) and EDX microanalyses of the regions labelled 1 and 2 in panel A (D).

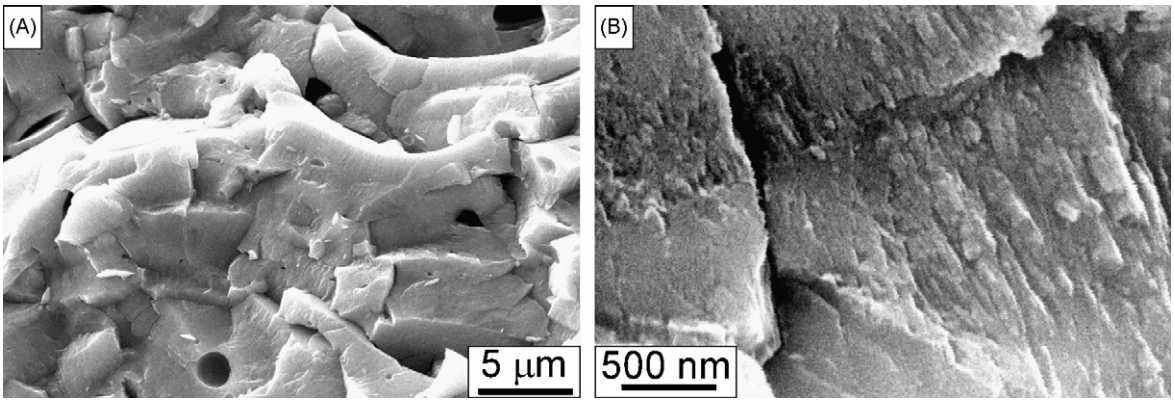

Fig. 3. SEM micrographs (secondary electrons) of the fracture surfaces of the as-deposited M coating: (A) low-magnification view and (B) high-magnification view.

to that reported for the solid-state synthesis of $BaFe_{12}O_{19}$ from oxides or from amorphous precursors.[18,19] The only difference is the presence of the Fe^{2+} in FeO, which is not a stable oxidation state of Fe. This can be explained by two factors. Firstly, the reducing atmosphere of the Ar–H_2 plasma jets is known to cause a partial reduction of oxide ceramics: the formation of Ti suboxides during the deposition of TiO_2 coatings or the partial reduction of Cr_2O_3 (with the possible appearance of metallic Cr in the coatings) are well-documented examples.[20–22] Secondly, the very rapid quenching of lamellae upon impact with the substrate favours the retention of metastable phases in thermally sprayed coatings.[23–26] Based on known thermodynamic data $BaFe_{12}O_{19}$ is the most stable compound at 727–1727 °C.[14,27] Above 1727 °C the Fe_3O_4 and FeO are in equilibrium with compounds having Fe/Ba = 2, 1, 2/3 or 2/5. For this reason it is most likely that the S peaks correspond to magnetite and not to γ-Fe_2O_3 (maghemite), which is an oxidized magnetite with a structure so similar to magnetite that they cannot be distinguished with the XRD.

The partial reduction of the original $BaFe_{12}O_{19}$ composition and the formation of a multi-phase system is reflected in the SEM micrographs of the coating's cross-section (Fig. 2A), exhibiting a layered microstructure with various shades of grey. EDX microanalysis, indeed, reveals that a higher or lower Ba/Fe ratio exists in the brighter or darker regions, respectively (Fig. 2B). Different phases are therefore present in different lamellae and also inside the same lamella, due to chemical and structural alterations occurring during the plasma-spraying process. It should also be noted that some rounded inclusions are sometimes present in the plasma-sprayed coatings (Fig. 2A). They might be either partially unmelted agglomerates (i.e., spherical spray-dried agglomerates that are not completely molten in the plasma jet) or re-solidified agglomerates (i.e., fully-molten droplets that are beginning to solidify before they impact on the substrate). As-spray-dried agglomerates are highly porous, they should retain a significant share of that porosity if they remain partially unmelted, and some of the micron-sized primary ferrite particles should still be recognizable, at least in the core of the agglomerate. By contrast, the spherical inclusions found in the present coatings (for details, see Figs. 2B and C) look quite dense, without any primary particle: they only possess a few spherical pores that originate from the entrainment of gas bubbles inside the molten material. Moreover, these rounded inclusions show a clear dendritic microstructure (Figs. 2B and C: dark dendrites surrounded by a bright matrix), which is a more strong evidence of a melt re-solidification process. The dark dendrites possess a radial orientation (Fig. 2C), i.e., they are directed from the periphery of the inclusion towards its centre. This is the obvious consequence of the re-solidification process: the crystalline phases nucleated on the droplet surface and then grew towards its core, along the heat-flow direction.

The EDX spectra reveal that the dark dendrites are iron-rich (with an EDX spectrum similar to the one shown for "area 1" in Fig. 2D). It should be noted that these dendrites are very small and that the corresponding EDX spectrum also includes some of the surrounding area. Therefore these dendrites may be pure Fe oxide or they may also contain a small fraction of Ba. We can conclude that both the dendrites and the surrounding bright (Ba-rich) matrix represent a frozen high-temperature phase equilibrium (see the preceding paragraph), which was retained due to the fast cooling: Fe_3O_4 and FeO are in equilibrium with compounds having Fe/Ba = 2, 1, 2/3 or 2/5 at temperatures above 1727 °C.

The above results show that the crystallization of the Ba hexaferrite was not completed during the deposition, neither inside the fully-molten lamellae which solidify upon impact with the substrate, nor in the partially re-solidified inclusions. The feedstock Ba hexaferrite powder melted completely during the spraying process. The fracture surface of Fig. 3A indeed exhibits many well-flattened lamellae, which are a clear sign of a high degree of melting of the feedstock powder. Such a degree of melting is further confirmed by the presence of some rounded pores, due to gas entrapment in the molten material, as seen in Fig. 3A. Furthermore, a coating primarily made up of fully-molten lamellae generally exhibits excellent interlamellar cohesion, resulting in a few longitudinal interlamellar defects, and several transverse intralamellar microcracks, due to the accumulation of quenching stresses in strongly adherent lamellae[28,29]; this is clearly confirmed by Fig. 2A. Once the melt is deposited on the substrate it cools down very quickly, with an approximate cooling rate of 10^7–10^9 K/s,[23,24] which severely hinders the complex, indirect crystallization process of the hexaferrite phase. Accordingly, high-magnification views of the fracture surface (Fig. 3B) reveal the presence of very small columnar grains (width ≤100 nm),

Table 2
Results from the TA analyses and the assigned chemical processes determined in a combination with the XRD analysis.

Temperature range (°C)	DSC peak	TGA	Chemical process
200–600	Exothermic	Mass increase	$5FeO \xrightarrow{O_2(g)} \alpha\text{-}Fe_2O_3 + Fe_3O_4$, $2Fe_3O_4 \xrightarrow{O_2(g)} 3\gamma\text{-}Fe_2O_3$
560–800	Exothermic	/	$\gamma\text{-}Fe_2O_3 \rightarrow \alpha\text{-}Fe_2O_3$
>800	Exothermic	/	$BaFe_2O_4 + 6\alpha\text{-}Fe_2O_3 \rightarrow BaFe_{12}O_{19}$

witnessing the high nucleation rate and slow grain-growth rate, typical of a significantly undercooled liquid. Under these conditions, a subsequent reaction between iron oxides and Ba-rich phases to form the thermodynamically stable hexaferrite is very difficult. We can conclude that the Ba hexaferrite phase only began to crystallize but the process was not finished since the coating cooled too quickly to room temperature. It is also possible that some of the Ba hexaferrite phase present comes from small amounts of unmelted material embedded in the coating. It has been shown previously that the crystallization of hexaferrites is a very slow process[30] and that other techniques for film preparation also require annealing.[31–35] The substrate temperature reached a maximum of 400 °C for these experiments; this is too low, if we consider that 600–900 °C[14] is necessary for the higher crystallinity of the hexaferrites.

In order to promote the crystallization of Ba hexaferrite the coatings were annealed. This was studied with thermal analyses (TA, Table 2) in combination with XRD (Fig. 4), and supported by magnetic data (Table 3). Knowing that the crystallization of $BaFe_{12}O_{19}$ is a highly kinetically dependent process the TA experiment was carried out with two different heating rates: 5 and 1 K/min. The major differences between the TA data obtained from the different heating rates were the temperatures and the width of the DSC peaks. The DSC peaks were broader and were detected at lower temperatures when a slower heating rate was used. The temperature ranges of the identified processes listed in Table 2 include the temperature ranges of both measurements. The TGA curve showed an increase in mass during the heating at 200–600 °C, while no significant mass difference at higher temperatures or during the cooling was detected. A broad exothermic peak was detected in the DSC curve over the same temperature range. To identify which chemical processes are related to the observed DSC peaks, samples were heated to various temperatures with heating rates of 5 and 1 K/min (the same as in the DSC measurements). Once the final temperature was reached the samples were pulled out from the furnace to be quickly cooled to room temperature. The XRD pattern of the sample heated to 485 °C (Fig. 4) is similar to the one of the as-deposited sample (Fig. 1). However, in addition to others, $\alpha\text{-}Fe_2O_3$ (hematite) peaks were also detected in the sample heated to 485 °C. At the same time, the relative intensities of the FeO (wuestite) peaks decrease with the heating temperature (see also Fig. 1). From this we can conclude that the low-temperature DSC peak corresponds to the oxidation of wuestite to hematite and of magnetite to maghemite. The magnetite cannot be distinguished from the maghemite in the XRD pattern since their crystal structures are so similar. Due to the paramagnetic/antiferromagnetic nature of both main oxide phases, wuestite and hematite, the maximum magnetization (M_{max}) values of the samples annealed at low temperatures are low (Table 3). The slight increase of the M_{max} measured for the sample annealed at 485 °C can only originate from the increasing amount of magnetite and/or maghemite. This suggests that FeO does not oxidize only to hematite but also to magnetite. Two additional exothermic peaks in the DSC curve were detected during the heating of the sample: at 560–800 °C and at >800 °C. The first peak corresponds to the transformation of maghemite to hematite, which usually takes place above 600 °C.[36] Consequently, the M_{max} value decreases again for the sample annealed at 700 °C. The high-temperature peak corresponds to the crystallization of the $BaFe_{12}O_{19}$. In accordance with this, the XRD pattern of the sample heated to 800 °C showed no obvious difference from the one heated to 485 °C. However, the XRD pattern of the sample heated to 900 °C showed very intense Ba

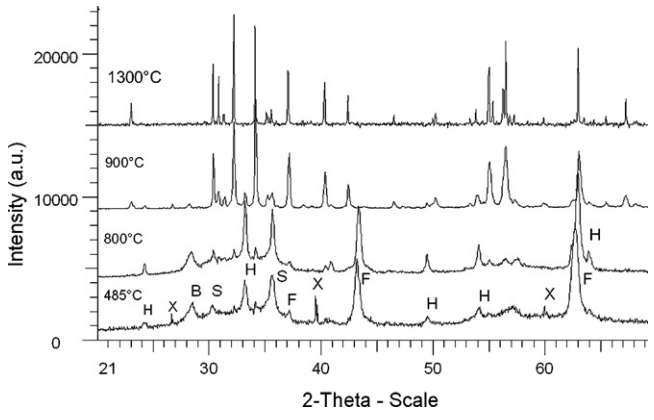

Fig. 4. XRD patterns of the Ba hexaferrite samples heated to various temperatures, where B denotes $BaFe_2O_4$, S denotes Fe_3O_4 and $\gamma\text{-}Fe_2O_3$, F denotes FeO, H denotes $\alpha\text{-}Fe_2O_3$, and X denotes peaks from the substrate. The unmarked peaks correspond to $BaFe_{12}O_{19}$ (μPDSM 84-0757).

Table 3
The magnetic properties of the as-deposited and annealed Ba hexaferrite coatings: magnetization measured with a maximum field of 1.2 T (M_{max}) and coercivity (Hc).

Annealing	M_{max} (emu/g)	Hc (Oe)
As-deposited	7.5	321
380 °C 1 h	6.1	374
485 °C 1 h	14.0	228
700 °C 1 min	4.8	234
800 °C 1.5 h	3.8	340
900 °C 1 min	26	2662
1000 °C 3 h	22	2970
1100 °C 3 h	58	3205
1200 °C 3 h	59	2230
1300 °C 3 h	58	651

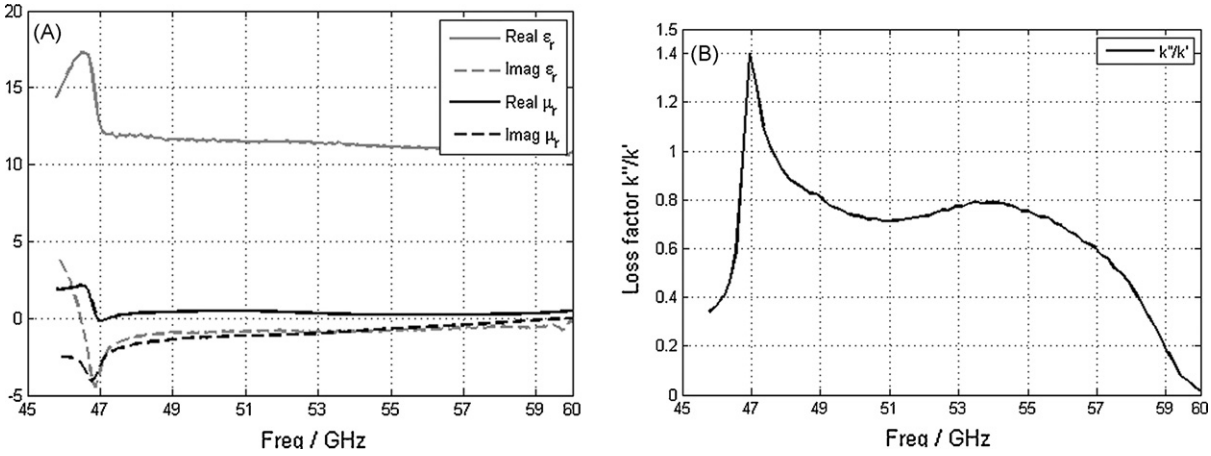

Fig. 5. Measured electromagnetic material parameters of the sintered Ba hexaferrite sample: (A) complex permittivity (ε_r) and permeability (μ_r), and (B) loss factor.

hexaferrite peaks. This was also consistent with the magnetic properties of these samples (Table 3). The M_{max} increased together with the coercivity (Hc) of the samples annealed above 800 °C due to the crystallization of $BaFe_{12}O_{19}$. No DSC peaks can be distinguished during the cooling, indicating that all the reactions were irreversible.

There is lack of kinetic data on the crystallization of $BaFe_{12}O_{19}$ from the melt. Nevertheless, similar findings were obtained here to those reported for the crystallization mechanism of $BaFe_{12}O_{19}$ from amorphous coprecipitates.[37] The coprecipitation study showed that the nucleation of $BaFe_{12}O_{19}$ is instantaneous and that the crystal growth via diffusion is the rate-determining step. Obviously, the small $BaFe_{12}O_{19}$ crystallites were present from the beginning and a high enough temperature was necessary for their growth. In addition to this, the already crystallized secondary phases (hematite, $BaFe_2O_4$) need to overcome a certain activation energy, i.e., a high enough temperature and a long enough time are required for the two to react and to form $BaFe_{12}O_{19}$. In order to obtain single-phase Ba hexaferrite coatings the annealing was carried out up to 1300 °C. The XRD pattern of the sample annealed at 1300 °C (Fig. 4) shows only the $BaFe_{12}O_{19}$ structure, with the very narrow XRD peaks indicating a high degree of crystallinity. The Hc value of 651 Oe (Table 2) is typical for $BaFe_{12}O_{19}$ with multidomain grains. The M_{max} value is 58 emu/g, which is in the range of the usually reported bulk values for the saturation magnetization (around 52–72 emu/g).[1,16,30] When the annealing temperature was decreased to 1100 and 1200 °C, the M_{max} value remained roughly the same, while the Hc value was higher, by several thousand Oe. This suggests that the Ba hexaferrite coatings annealed at 1100 and 1200 °C contained only a small fraction of multidomain grains and the rest are still in the single-domain state.

Another Ba hexaferrite sample, which was prepared with different processing parameters on a glass substrate (see Section 2), showed similar crystallization behaviour to that described above. From this we can conclude that the APS process does not provide enough time for the recrystallization of $BaFe_{12}O_{19}$. Instead, annealing above 1000 °C was required to obtain single-phase crystalline coatings. Nevertheless, the formation of the single-phase coatings proves that there was no significant loss of cations during the APS process.

The measured electromagnetic properties of the sintered Ba hexaferrite are shown in Fig. 5. Fig. 5A shows the measured complex permittivity (ε_r) and the permeability (μ_r), where the ferromagnetic resonance of the Ba hexaferrite sample is shown clearly at 46.5 GHz. At the ferromagnetic resonance the real part of the permeability drops rapidly and the imaginary part (magnetic losses) reaches its highest value. Fig. 5B shows the measured dissipation factor or loss factor. The loss factor is the ratio between the imaginary and the real parts of the propagation factor ($Im(\sqrt{\mu\varepsilon})/Re(\sqrt{\mu\varepsilon})$). The Ba hexaferrite sample has very high losses at the ferromagnetic resonance, which is seen as a high peak in the loss factor. The high losses caused problems with the measurement accuracy, which can be seen as a peak in the measured permittivity in Fig. 5A. The transmission loss through the 0.47-mm-thick bulk sample was over 25 dB. The calculations based on ε_r and μ_r showed that the reflection from the coated metal plate has its minimum when the coating thickness is 0.15–0.25 mm at 46 GHz, when only a few percent of the incoming power is reflected backwards.

3.2. The Ba-CoTi hexaferrite coatings

Fig. 6 shows the XRD patterns of the feedstock Ba-CoTi hexaferrite feedstock powder and the as-deposited coating. The XRD peaks of the Ba hexaferrite and the magnetite structures can be identified in the XRD pattern of the as-deposited Ba-CoTi hexaferrite coating. In contrast to the Ba hexaferrite coatings the degree of crystallization of the Ba-CoTi hexaferrite was extensive during the deposition (see Section 3.1). A possible explanation for this obvious difference is the following. The results on Ba hexaferrite coatings showed that fully molten droplets could not form the hexaferrite phase, neither upon impact quenching, nor during in-flight re-solidification. The deposition parameters for the Ba-CoTi hexaferrite coating (Table 1) were therefore chosen in order to limit the heating of the agglomerates during spraying, so that some more unmelted material was retained in the as-deposited coating. This coating accordingly retained more crystalline hexaferrite phase than the

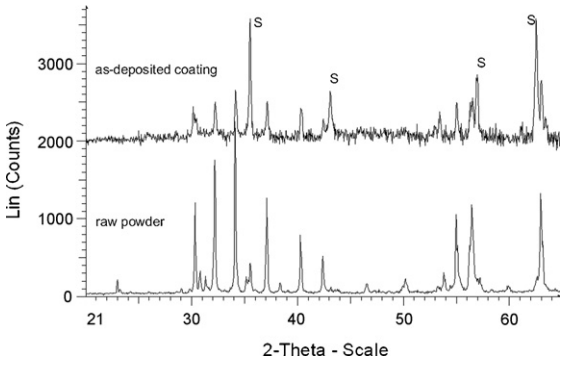

Fig. 6. XRD patterns of the raw Ba-CoTi hexaferrite powder and the as-deposited coating. S denotes the magnetite structure. The unmarked peaks correspond to the Ba hexaferrite structure (μPDSM 84-0757).

Ba hexaferrite coating examined in the previous section (see Section 3.1)

The presence of the magnetite peaks in the as-deposited coating (Fig. 6) could be a consequence of Ba loss during the spraying as was concluded by Vidal and Taylor.[14] However, this was not the case here. The formation of single-phase coatings after annealing suggests that no significant loss of Ba occurred during the APS. Fig. 7 shows the XRD patterns of the samples annealed for 3 h. A similar explanation is valid here as in the case of the Ba hexaferrite coatings (see Section 3.1). The formation of hematite (α-Fe_2O_3) from maghemite (γ-Fe_2O_3) takes place at a minimum of 600 °C.[36] This can also be seen from the XRD data, where the intensities of the hematite peaks increase at the expense of the magnetite/maghemite peaks, with the annealing temperature. Finally, the samples annealed at 800 °C show only peaks corresponding to the Ba hexaferrite and hematite structures. The relative intensity of the hematite peak decreases with a further increase of the annealing temperature (i.e., at 900 °C). Diffractograms of the samples annealed at 1000–1200 °C were not included in Fig. 7 for the sake of clarity. They are similar to the diffractogram of the sample annealed at 900 °C. The single-phase Ba-CoTi hexaferrite coatings were obtained after annealing at 1300 °C for 3 h. A slight shift in the 2-theta values of the Ba hexaferrite peaks with respect to the XRD patterns

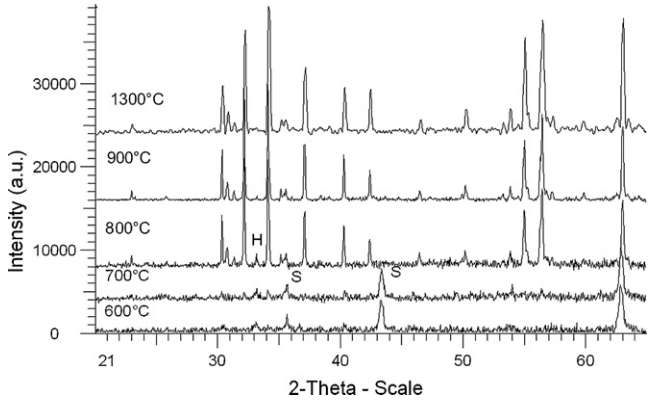

Fig. 7. XRD patterns of the samples annealed for 3 h at various temperatures. S denotes maghemite, H denotes hematite and the unmarked peaks correspond to the Ba hexaferrite structure (μPDSM 84-0757).

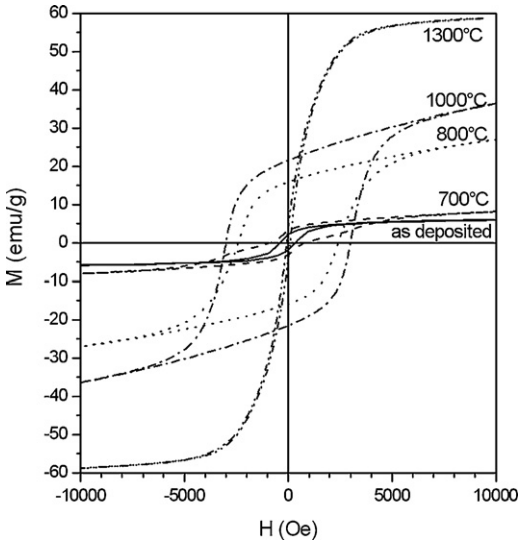

Fig. 8. Hysteresis loops of the Ba-CoTi hexaferrite coatings.

of the samples annealed below 1300 °C indicates the difference in the crystal-lattice sizes. The latter must originate from the different degree of Fe^{3+} substitution with $Co^{2+}Ti^{4+}$.

The evolution of the magnetic behaviour of the Ba-CoTi hexaferrite coatings with the annealing temperature is shown in Fig. 8. The hysteresis curves of the samples annealed below 800 °C show a kind of double-S shape, which is typical for samples containing two magnetic phases. This is in accordance with the XRD data (Fig. 7), where the magnetite and hexaferrite structures were detected in the corresponding coatings. The M_{max} and Hc values are small and increase significantly for the samples annealed at ≥800 °C due to the crystallization of the hexaferrite phase. However, these samples were not completely saturated at the maximum applied field of 1.2 T, as can be seen in Fig. 8. This is consistent with their large anisotropy field, which further results in large Hc values, typical for pure $BaFe_{12}O_{19}$. Namely, the Hc values increased from 2400 to 3000 Oe as the annealing temperature increased from 800 to 1000 °C. This suggests that the chemical composition of the hexaferrite phase detected with the XRD in the samples annealed at 800–1000 °C is not $BaCoTiFe_{10}O_{19}$. The substitution of the Fe^{3+} with the $Co^{2+}Ti^{4+}$ reduces the magnetocrystalline anisotropy field and at $x \sim 1$ the uniaxial anisotropy switches to planar.[2,40] Consequently, the coercivity within the plane becomes very low. The Hc value started to decrease when the annealing temperature increased above 1000 °C and reached a minimum of 82 Oe when the coatings were annealed at 1300 °C. Such a low Hc value[38,39] suggests that the chemical composition of these coatings was indeed $BaCoTiFe_{10}O_{19}$. This is also consistent with the high M_{max} value, 59 emu/g, measured on the coatings annealed at 1300 °C. We can conclude that no significant mass loss for any of the cations occurred during the APS process and the APS technique can also be used for the preparation of CoTi-substituted Ba hexaferrite coatings.

The measured electromagnetic properties of the Ba-CoTi hexaferrite ceramic samples and the reflection of the respective coatings were obtained in the same way as for the Ba hexafer-

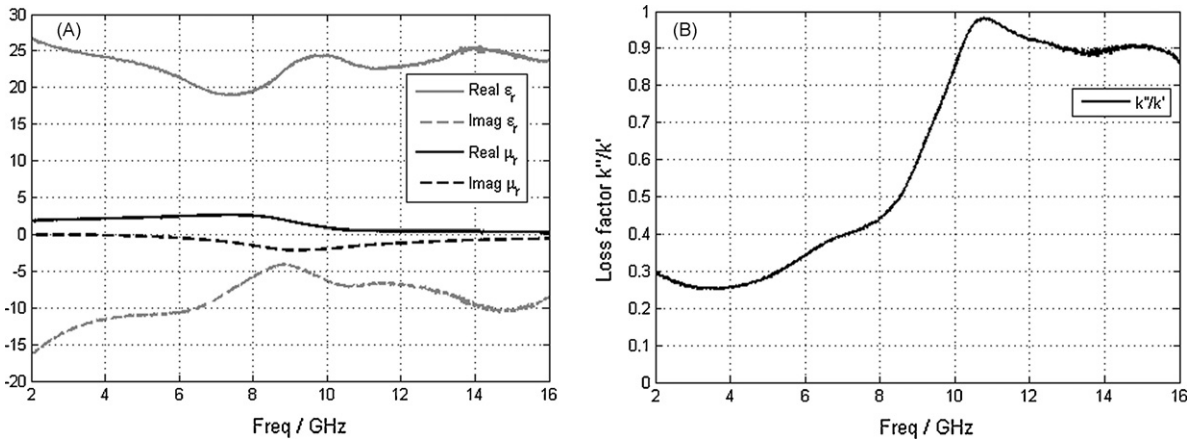

Fig. 9. Measured electromagnetic material parameters of the sintered Ba-CoTi hexaferrite sample (A) complex permittivity (ε_r) and permeability (μ_r), (B) loss factor.

rite, except that the Ba-CoTi hexaferrite sample was placed in a coaxial waveguide holder. The measured permeability and the permittivity are shown in Fig. 9A. The ferromagnetic resonance of the Ba-CoTi hexaferrite material can be seen at 9 GHz. The loss factor (Fig. 9B) is not as high as for the Ba hexaferrite material (Fig. 5B) and it reaches its maximum near the ferromagnetic resonance. Our calculations have shown that the reflection from the coated metal plate has a minimum when the coating thickness is 1–4 mm at a frequency range 3–9 GHz, when less than 10% of the incoming power is reflected backwards.

4. Conclusions

Thick hexaferrite coatings with compositions of $BaFe_{12}O_{19}$ and $BaCoTiFe_{10}O_{19}$ were prepared with atmospheric plasma spraying technology. The feedstock powder melted completely and formed a semi-crystalline precursor on the glass substrate. The degree of crystallization of the $BaCoTiFe_{10}O_{19}$ was significantly higher than that of the $BaFe_{12}O_{19}$. Annealing above 1000 °C was necessary for the complete crystallization of both compositions. No significant loss of any metal ion occurred during the APS process. $BaFe_{12}O_{19}$ and $BaCoTiFe_{10}O_{19}$ coatings with thicknesses of 0.15–0.25 mm and 1–4 mm, respectively, showed electromagnetic properties suitable for mm- and microwave absorbing applications. Coatings of an appropriate thickness were prepared in this study, and we have shown that APS is a promising technology for the production of absorbent coatings.

Acknowledgements

This work was carried out in the frame of the EU6, MATERA ERA-NET, 4302-31/2006/26, ABSOFILM project with the financial support of the Ministry for Higher Education, Science and Technology of the Republic of Slovenia, Tekes, the Finnish Funding Agency of Technology and Innovation, the Ministry of Innovation, Science, Research and Technology of the State of North Rhine-Westphalia of Germany, and INRIM.

References

1. Smit, J. and Wijn, H. P. J., *Ferrites*. Philips' Technical Library, Eidenhoven, 1959, Chapter IX.
2. Brard, C., Taffary, T., Autissier, D. and Jorion, F., Influence on Fe^{2+} on microwave behavior of $M(Co, Ti)_{1.2}$ type hexaferrite. *J. Phys. IV France*, 1998, **8**, Pr2-401–Pr2-404.
3. Vincent, H., Sugg, B., Lefez, V., Bochu, B., Boursier, D. and Chaudouet, P., Crystal growth, X-ray and magnetic studies of planar anisotropy M-hexaferrites $BaFe_{12-2x}Ir_xMe_xO_{19}$ (Me = Zn, Co). *J. Magn. Magn. Mater.*, 1991, **101**, 170–172.
4. Zhou, X. Z., Morrish, A. H., Yang, Z. and Zeng, H.-X., Co-Sn substituted barium ferrite particles. *J. Appl. Phys.*, 1994, **75**, 5556–5558.
5. Du Pre, F. K., De Bitetto, D. J. and Brockman, F. G., Magnetic materials for use at high microwave frequencies (50-90 kMc/sec). *J. Appl. Phys.*, 1958, **9**, 1127–1128.
6. Sugimoto, S., Haga, K., Kagotani, T. and Inomata, K., Microwave absorption properties of Ba-M type ferrite produced by a modified coprecipitation method. *J. Magn. Magn. Mater.*, 2005, **290–291**, 1188–1191.
7. Li, Z. W., Chen, L. and Ong, C. K., Studies of static and high-frequency magnetic properties for M-type ferrite $BaFe_{12-2x}Co_xZr_xO_{19}$. *J. Appl. Phys.*, 2002, **92**, 3902–3907.
8. Heimann, R. B., Applications of plasma-sprayed ceramic coatings. *Key Eng. Mater.*, 1996, **122-124**, 399–442.
9. Herman, H., Sampath, S. and McCune, R., Thermal spray: current status and future trends. In *Thermal Spray Processing of Materials: MRS Bulletin – July 2000,*, ed. S. Sampath and R. McCune. Material Research Society, Warrendale, PA, USA, 2000, pp. 17–25.
10. Bartuli, C., Cipri, F. and Valente, T., Thermal spraying and the fabrication of coatings with tailored electro-magnetic properties. *Inorg. Chim. Acta*, 2008, **361**, 4077–4088.
11. Ge, S., Ma, X., Zhang, T., Wu, M., Zhang, H., Zhang, Y. D., Ings, J. and Yacaman, J., Structural and magnetic properties of nanostructured $Ni_{0.5}Zn_{0.5}Fe_2O_4$ films fabricated by thermal spray. *J. Appl. Phys.*, 2003, **93**, 7498–7500.
12. Yan, Q. Y., Gambino, R. J., Sampath, S. and Huang, Q., Neutron diffraction and ferromagnetic resonance studies on plasma-sprayed MnZn ferrite films. *J. Appl. Phys.*, 2005, **97**, 0033902-1–0033902-7.
13. Yan, Q., Gambino, R. J., Sampath, S., Lewis, L. H., Li, L., Baumberger, E., Vaidya, A. and Xiong, H., Effects of zinc loss on the magnetic properties of plasma-sprayed MnZn ferrites. *Acta Mater.*, 2004, **52**, 3347–3353.
14. Vidal, E. E. and Taylor, P. R., Thermal plasma synthesis of $BaFe_{12}O_{19}$ (BaM) films. *Plasma Chem. Plasma Proc.*, 2003, **23**(4), 609–626.
15. Salahun, E., Queffelec, P., Tanne, G., Adenot, A.-L. and Acher, O., Correlation between magnetic properties of layered ferromagnetic/dielectric

materials and tunable device applications. *J. Appl. Phys.*, 2002, **91**, 5449–5455.
16. Cho, H. S. and Kim, S. S., M-hexaferrites with planar magnetic anisotropy and their applications to high-frequency microwave absorbers. *IEEE Trans. Magn.*, 1999, **35**, 3151–3153.
17. Hewlett-Packard *Product Note 8510-3*, 1985.
18. Carp, O., Barjega, R., Segal, E. and Brezeanu, M., Nonconventional methods for obtaining hexaferrites II. Barium hexaferrite. *Thermochim. Acta*, 1998, **318**, 57–62.
19. Goto, Y. and Takada, T., Phase diagram of the system BaO-Fe_2O_3. *J. Am. Ceram. Soc.*, 1960, **43**, 150–153.
20. Skopp, A., Kelling, N., Woydt, M. and Berger, L.-M., Thermally sprayed titanium suboxide coatings for piston ring/cylinder liners under mixed lubrication and dry-running conditions. *Wear*, 2007, **262**, 1061–1070.
21. Wang, X. Y., Liu, Z., Liao, H., Klein, D. and Coddet, C., Deoxidization and phase analysis of plasma sprayed TiO2 by X-ray Rietveld method. *Thin Solid Films*, 2005, **473**, 177–184.
22. Vippola, M., Vuorinen, J., Vuoristo, P., Lepistö, T. and Mäntylä, T., Thermal analysis of plasma sprayed oxide coatings sealed with aluminium phosphate. *J. Eur. Ceram. Soc.*, 2002, **22**, 1937–1946.
23. Fauchais, P., Fukumoto, M., Vardelle, A. and Vardelle, M., Knowledge concerning splat formation: an invited review. *J. Thermal Spray Technol.*, 2004, **13**, 337–360.
24. Bianchi, L., Denoirjean, A., Blein, F. and Fauchais, P., Microstructural investigation of plasma-sprayed ceramic splats. *Thin Solid Films*, 1997, **299**, 125–135.
25. Li, L., Kharas, B., Zhang, H. and Sampath, S., Suppression of crystallization during high velocity impact quenching of alumina droplets: observations and characterization. *Mater. Sci. Eng. A*, 2007, **456**, 35–42.
26. Crawmer, D. E., Coating structures, properties and materials. In *Handbook of Thermal Spray Technology*, ed. J. R. Davis. ASM International, Material Park, OH, USA, 2004, pp. 47–53.
27. Pouillard, G., Alam, M. S., Dufour, M. C. T. and Perrot, P., The binary system oxide-iron(III) oxide (BaO-Fe_2O_3): phase diagram and thermodynamic properties. *J. Chem. Res. (M)*, 1981, 1720–1747;
Pouillard, G., Alam, M. S., Dufour, M. C. T. and Perrot, P., The binary system oxide-iron(III) oxide (BaO-Fe_2O_3): phase diagram and thermodynamic properties. *J. Chem. Res. (S)*, 1981, 136–137.
28. Sevostianov, I., Kachanov, M., Ruud, J., Lorraine, P. and Dubois, M., Quantitative characterization of microstructures of plasma-sprayed coatings and their conductive and elastic properties. *Mater. Sci. Eng. A*, 2004, **386**, 164–174.
29. Matejicek, J., Sampath, S., Gilmore, D. and Neiser, R., In situ measurement of residual stresses and elastic moduli in thermal sprayed coatings. Part 2: Processing effects on properties of Mo coatings. *Acta Mater.*, 2003, **51**, 873–885.
30. Sudakar, C., Subbannna, G. N. and Kutty, T. R. N., Nanoparticles of barium hexaferrite by gel to crystalline conversion and their magnetic properties. *J. Electroceram.*, 2001, **6**, 123–134.
31. Diaz-Castanon, S., Sanchez, J. L., Leccabue, L. F., Watts, B. E., Garcia, T. and Deposada, E., Magnetic properties of polycrystalline hexaferrites thin films grown by metal-organic decomposition and pulsed laser deposition: an useful correlation. *Mater. Sci. Forum*, 1999, **302–303**, 416–420.
32. Sui, X. and Kryder, M. H., Microstructural origin of the perpendicular anisotropy in M-type barium hexaferrite thin films deposited by rf magneton sputtering. *IEEE Trans. Magn.*, 1983, **29**, 3751–3752.
33. Lacroix, E., Gerard, P., Marest, G. and Dupuy, M., Substrate effects on the crystalline orientation of barium hexaferrite films. *J. Appl. Phys.*, 1991, **69**, 4770–4772.
34. Carparo, S., Chatelon, J. P., Joisten, H., Le Berre, M., Bayard, B., Barbier, D. and Rousseau, J. J., Magnetic properties of sputtered barium ferrite thick films. *J. Appl. Phys.*, 2003, **93**, 9898–9901.
35. Pramanik, N. C., Fujii, T., Nakanishi, M. and Takada, J., Development of nanograined hexagonal barium ferrite thin films by sol-gel technique. *Mater. Lett.*, 2005, **59**, 468–472.
36. Ogasawara, T. and Oliviera, M. A. S., Microstructure and hysteresis curves of the barium hexaferrite from co-precipitation by organic agent. *J. Magn. Magn. Mater.*, 2000, **217**, 147–154.
37. Lisjak, D. and Drofenik, M., The mechanism of the low temperature formation of barium hexaferrite. *J. Eur. Ceram. Soc.*, 2007, **27**, 4515–4520.
38. Ogata, Y., Iimura, T. and Harada, H., Fine particles of hexagonal ferrite for perpendicular recording media. *Adv. Ceram.*, 1984, **16**(Part II), 289–293.
39. Zhou, X. Z., Morrish, A. H., Li, Z. W. and Hong, Y. K., Site preference for Co^{2+} and Ti^{4+} in Co-Ti substituted barium ferrite. *IEEE Trans. Magn.*, 1991, **27**, 4654–4656.
40. Kreisel, J., Vincet, H., Tasset, F., Pate, M. and Gane, J. P., An investigation of the magnetic anisotropy change in $BaFe_{12-2x}Ti_xCo_xO_{19}$ single crystals. *J. Magn. Magn. Mater.*, 2001, **224**, 17–29.